Multiphoton imaging for morphometry of the sandwich-beam structure of the human stapedial annular ligament

Schär, Merlin ; Dobrev, Ivo ; Chatzimichalis, Michail ; Röösli, Christof ; Sim, Jae Hoon

Abstract: Background The annular ligament of the human stapes constitutes a compliant connection between the stapes footplate and the peripheral cochlear wall at the oval window. The cross section of the human annular ligament is characterized by a three-layered structure, which resembles a sandwich-shaped composite structure. As accurate and precise descriptions of the middle-ear behavior are constrained by lack of information on the complex geometry of the annular ligament, this study aims to obtain comprehensive geometrical data of the annular ligament via multiphoton imaging. Methods The region of interest containing the stapes and annular ligament was harvested from a fresh-frozen human temporal bone of a 46-years old female. Multiphoton imaging of the unstained sample was performed by detecting the second-harmonic generation of collagen and the autofluorescence of elastin, which are constituents of the annular ligament. The multiphoton scans were conducted on the middle-ear side and cochlear side of the annular ligament to obtain accurate images of the face layers on both sides. The face layers of the annular ligament were manually segmented on both multiphoton scans, and then registered to high-resolution CT images. Results Multiphoton scans of the annular ligament revealed 1) relatively large thickness of the core layer compared to the face layers, 2) asymmetric geometry of the face layers between the middle-ear side and cochlear side, and variation of their thickness and width along the footplate boundary, 3) divergent relative alignment of the two face layers, and 4) different fiber composition of the face layers along the boundary with a collagen-reinforcement near the anterior pole on the middle-ear side. Conclusion and outlook Multiphoton microscopy is a feasible approach to obtain the detailed three-dimensional features of the human stapedial annular ligament along its full boundary. The detailed description of the sandwich-shaped structures of the annular ligament is expected to contribute to modeling of the human middle ear for precise simulation of middle-ear behavior. Further, established methodology in this study may be applicable to imaging of other middle-ear structures. Keywords Annular ligament Stapes Multiphoton microscopy Two-photon microscopy Face layer Core layer

DOI: https://doi.org/10.1016/j.heares.2018.11.011

Originally published at:
Schär, Merlin; Dobrev, Ivo; Chatzimichalis, Michail; Röösli, Christof; Sim, Jae Hoon (2019). Multiphoton imaging for morphometry of the sandwich-beam structure of the human stapedial annular ligament. Hearing Research, 378:63-74.
DOI: https://doi.org/10.1016/j.heares.2018.11.011

MULTIPHOTON IMAGING FOR MORPHOMETRY OF THE SANDWICH-BEAM STRUCTURE OF THE HUMAN STAPEDIAL ANNULAR LIGAMENT

Schär M[1,2], Dobrev I[1,2], Chatzimichalis M[3], Röösli C[1,2], Sim JH[1,2]

[1] Department of Otorhinolaryngology, Head and Neck Surgery, University Hospital Zurich, Frauenklinikstrasse 24, 8095 Zürich, Switzerland

[2] University of Zurich, Rämistrasse 71, 8006, Zürich, Switzerland

[3] Dorset County Hospital, Williams Ave, Dorchester, Dorset, United Kingdom

Hearing Research 378: 63-74, 2019

Highlights

- Multiphoton microscopy was used to obtain detailed geometry of the annular ligament of the human stapes
- The annular ligament of the human stapes features a three-layered structure with the thickness and width varying along the boundary.
- The face layers of the annular ligament are relatively thin compared to the core layer.
- The three-layered structure of the annular ligament is efficient for providing bending stiffness.
- The established methodology in this study may be applicable to imaging of other middle-ear structures

Abstract

Background: The annular ligament of the human stapes constitutes a compliant connection between the stapes footplate and peripheral cochlear wall at the oval window. The cross section of the human annular ligament is characterized by a three-layered structure, which resembles a sandwich-shaped composite structure. As accurate and precise descriptions of the middle-ear behavior are constrained by lack of information on the complex geometry of the annular ligament, this study aims to obtain comprehensive geometrical data of the annular ligament via multiphoton imaging.

Methods: The region of interest containing the stapes and annular ligament were harvested from a fresh-frozen human temporal bone of a 46-years old female. Multiphoton imaging of the unstained sample was performed by detecting the second-harmonic generation of collagen and the autofluorescence of elastin, which are constituents of the annular ligament. The multiphoton scanning was conducted on the middle-ear side and cochlear side of the annular ligament to obtain accurate images of the face layers on both sides. The face layers of the annular ligament were manually segmented on both multiphoton scans, and then registered to high-resolution μCT images.

Results: Multiphoton scans of the annular ligament revealed 1) relatively large thickness of the core layer compared to the face layers, 2) asymmetric geometry of the face layers between the middle-ear side and cochlear side and variation of their thickness and width along the footplate boundary, 3) divergent relative alignment of the two face layers, and 4) different fiber composition of the face layers along the boundary with a collagen-reinforcement near the anterior pole on the middle-ear side.

Conclusion and outlook: Multiphoton microscopy is a feasible approach to obtain the detailed three-dimensional features of the human stapedial annular ligament along its full boundary. The detailed description of the sandwich-shaped structures of the annular ligament is expected to contribute to modeling of the human middle ear for precise simulation of middle-ear behavior. Further, established methodology in this study may be applicable to imaging of other middle-ear structures.

Keywords: Annular ligament, stapes, multiphoton microscopy, two-photon microscopy, face layer, core layer

1. Introduction

The stapedial annular ligament (AL) provides a compliant ring-shaped connection between the stapes footplate and the peripheral cochlear wall at the oval window. The stapedial motion and the resulting effective stimuli to the cochlea are considerably influenced by mechanical properties of the AL, especially pathological changes in the material structure such as ligamentary stiffening due to otosclerosis. Further reflecting its clinical importance, pretension of the AL in ossicular reconstructive surgery has been proposed as a crucial factor influencing postoperative outcome (Neudert et al. 2016). Therefore, an accurate and precise description of the AL is essential for numerical modeling of the human middle-ear under various conditions. However, this endeavor has been hampered due to lack of anatomical data of the AL, which has been known to feature a pronounced asymmetry with complex microstructures.

The detailed composition of the AL has been revealed mainly via conventional light microscopy (Davis 1948, Harty 1953, Brunner 1954, Gussen 1964), immunohistochemistry (Takanashi et al. 2013), or electron microscopy (Bolz and Lim 1972, Graham 1985). The studies showed that the human AL consists of two fiber-rich face layers and a core of lower fiber density between the fiber-rich layers. Therefore, cross sections of the AL expose structures with close similarity to sandwich beams. Sandwich beams, a subtype of mechanical composite structures, consist of two thin face layers of high mechanical strength which are coupled, with strong adhesive, to a thicker core layer of lower mechanical strength. These structures exhibit an interesting property that a higher bending stiffness can be achieved by solely increasing the distance between the face layers (i.e., increasing the thickness of the core layer) while keeping the thickness of the face layers constant (Zenkert 1997). This means that the sandwich structure of the AL, with the same amount of fibers, can achieve a higher bending stiffness than single-layer structures. Though the microscopy-based studies succeeded in qualitatively showing the detailed structures of the AL, they did not provide quantitative information of the complete ligament in 3D space. Quantitative data were reported in some studies, but they were usually obtained only at a few locations, and/or the locations and angular alignment of the microtome section planes relative to an anatomical coordinates system were not precisely defined.

To obtain quantitative information of the complete AL, μCT imaging has been used. Dimensions at several distinct locations were reported using μCT imaging in works by de Greef (2015) and Mohammadi et al. (2017). Baek et al. (2015) obtained the complete map of the thickness and width of the ligament along the full footplate boundary from μCT images. However, although μCT imaging has become an indispensable tool for several applications in

middle-ear research, the different layers of the AL are not distinguishable due to an inherently low soft-tissue contrast. In the work by Baek et al., the AL was modeled with bi-layered tapered Euler-Timoshenko beams, but the face layer thickness was only represented by a uniform thickness of 20 μm due to absence of the thickness profile along the entire footplate boundary.

As an alternative to μCT imaging, detailed three-dimensional features of the human AL may potentially be acquired from volumetric reconstructions of histological slices. However, this approach has significant drawbacks including: 1) sample shrinkage resulting from the exposure to various chemical agents during tissue processing, and 2) inhomogeneous artifact patterns across slices due to cutting. Such artifacts make it difficult to obtain a faithful reconstruction of the original spatial dimensions of the complete AL structure. Furthermore, histology requires significant time commitment for the case of very thin cutting series and large sample numbers.

This proof-of-concept study intends to introduce multiphoton microscopy as a new imaging modality for morphometry of the middle ear, overcoming limitations of other techniques currently used for middle-ear imaging. Multiphoton microscopy is a non-destructive optical imaging method which allows optical slicing of intact tissue based on a nonlinear optical effect from a pulsed combination of two (or more) photons. This approach enables use of longer wavelengths for fluorophore or tissue excitation, and therefore deeper tissue penetration. Since the excitation intensity is strong enough only in the focal point, no out-of-focus signal is generated. The face layers of the AL, which consist of elastin and collagen, could be imaged by the autofluorescence of elastin and second-harmonic generation of collagen. Thereby, the asymmetrical geometry of an intact stapedial AL with the detailed multi-layered structure was obtained, and dimensions of the face layers and core layer were measured with optical sectioning at sub-micron levels.

2. Materials and Methods

2. 1 Sample preparation

A fresh-frozen temporal bone (extraction within 48-72 hours after death) from the right side of a 46-years old female subject was used for this investigation. The sample was obtained from a certified tissue bank (Science Care Inc., Phoenix, AZ, USA), and the study was conducted under the ethical approval by the Ethic Committee of the Canton of Zurich (KEK submission No. 2014-0544).

The first step of temporal bone preparation involved a wide mastoidectomy and posterior tympanotomy to open the middle-ear cavity. Then, the incudostapedial joint was carefully disconnected, and the lateral part of the temporal bone including the tympanic membrane and malleus-incus complex above the stapes was removed. Subsequently, the medial side of the footplate was exposed by drilling through the internal auditory canal. Additionally, peripheral structures were removed, and both the medial and lateral side of the sample were extensively flattened to enable a sufficiently close access of the multiphoton objective within its maximal working distance of 2.6 mm. Great care was taken not to induce any damage to the AL. The resultant small sample, containing the stapes, the AL, and a small piece of surrounding temporal bone, was extracted, and the edges of the extracted sample were carefully attached to a metal plate by a UV curable adhesive (Blufixx GmbH, Wesseling, Germany). This technique resulted in very rigid but reversible attachment, which allowed fine drilling and preparation even very close to the delicate structures of the stapes footplate and the AL. In the last step, the stapedial tendon and both crura were cut using a Diode Pumped Solid State (DPSS) laser (Ceralas G5, Biolitec AG, Bonn, Germany). The sample was fixated in 4% paraformaldehyde, which served as a storage medium between preparation and imaging sessions.

2.2 Multiphoton microscopy

Multiphoton imaging was performed using a Leica TCS SP8 upright MP FLIM system (Leica Mikrosysteme Vertrieb GmbH, Wetzlar, Germany) with an HC IRAPO motCORR objective (25x magnification, NA 1.0, water immersion). The sample held on the metal plate was immersed into phosphate-buffered saline in a petri dish and placed on the standard sample holder of the microscope. This sample holder was mounted on a motorized movable base plate to allow in-plane (*XY*-plane) translation of the sample. The height of the objective along an axis perpendicular to the base plate (*Z*-axis) was adjustable as well by a third motorized stage. For multiphoton excitation, an Insight DS+ Dual ultrafast near-infrared laser (680-1300 nm tuning range) was tuned to an excitation wavelength (λ) of 880 nm. A constant laser intensity was

maintained for all scans. Signals were measured by two super-sensitive HyD detectors with a second-harmonic generation filter cube. During the image acquisition procedure, both detectors were set to photon counting mode. The range and peak sensitivity of the two detectors matched the emitted signals generated by autofluorescence of elastin and second harmonics of collagen.

The imaging of the face layers was conducted in two separate sessions from the medial and lateral sides, respectively because tissue penetration of photons from one side of the sample was too small to visualize both face layers. The face layer on the lateral side (i.e., side of the middle-ear cavity) was segmented in the images of the session from the lateral side, and the face layer on the medial side was segmented in the images of the session from the medial side.

For each of the two scans from the medial and lateral sides, the imaging procedures were performed with following three steps because the size of the sample (order of millimeters) exceeded the in-plane field of view of the multiphoton microscope used in this study (a square of 350 microns).

(1) Configuring the region of interest,

(2) Preliminary low-resolution scan, and

(3) High-resolution scan.

(1) Configuring the region of interest: Since the in-plane field of view of a multiphoton microscope is limited to a square of 350 microns, it is impractical to find the region of interest during multiphoton scanning. The approximate boundary of the footplate on the XY-plane was therefore obtained by imaging of the sample under white light illumination with a built-in Leica DFC7000 T Color CCD camera. The range of the region of interest along the Z-axis (the axis perpendicular to the base plate) was approximated by the range in which the contour appeared in focus.

(2) Preliminary low-resolution scan: After identifying the boundary of the footplate in the reference frame of the microscope, a preliminary low-resolution scan was performed to evaluate the accuracy of the estimated region of interest. The power intensity and resolution (6 microns in the X- and Y-direction and 5.4 microns in the Z-direction) were determined such that a good visibility of the ligamentary structures was obtained. The scan of the complete AL was performed by combining (stitching) sub-region scans with the maximal field of view (a square of 350 microns). The region of interest on the middle-ear side was tiled by 58 squares while 54 squares were used to tile the region of interest on the cochlear side. Then, stitching was necessary to merge the separately scanned squares to a continuous image of the whole scanning area. There was a 10% (area) overlap at the borders with neighboring sub-regions. This overlap facilitated the built-in stitching algorithm, which was running during image acquisition based

on the position information from the stages. The scanning depth along the Z-direction was given by the Z-range estimated in the previous step. In the case that the AL was not completely covered by the scanning region, the low-resolution scan was repeated with adjustment of the scanning region.

(3) High-resolution scan: Once coverage of the complete AL was confirmed in the low-resolution scan, the high-resolution scan was performed with a resolution of 692 nm in the X- and Y-directions and a resolution of 990 nm in the Z-direction. This resolution resulted in a scanning time of up to 11 hours for the currently used sample.

2.3 µCT imaging

Since multiphoton microscopy was performed separately for the medial and lateral sides of the footplate, µCT images for the sample were obtained for co-registration of the two multiphoton microscopy datasets. A substantial volume of the footplate and the temporal bone were included in the multiphoton microscopy to assist surface matching of multiphoton images to µCT data without the use of fiducial markers. The µCT scan was performed using a VivaCT-40 µCT scanner (SCANCO Medical AG, Switzerland). To obtain stable positioning of the small and delicate sample without damage, it was attached to a thin capillary tube after detachment from the metal holding plate, and the assembly was fixed in the cylindrical µCT sample holder. The free end of the capillary tube was used to fix the sample in the holder by expandable foam to avoid motion artifacts. The sample was immersed in phosphate-buffered saline during the complete scanning time. The photon energy level of the x-ray tube was set to 55 keV, and the voxel size of the reconstructed images was 6 microns (i.e., a cube of 6 microns).

2.4 Image processing

The two multiphoton datasets, one from each side of the footplate, and the µCT dataset were imported to Amira 6.4 (Thermo Fisher Scientific, Waltham, Massachusetts, USA). Due to large overlapping areas across the multiphoton scans and the µCT, the datasets could be co-registered using a surface-matching algorithm (Align Surface module in Amira). Subsequently, the two face layers of the AL were segmented from the multiphoton images, by manually outlining the face layers on slices. Then, surface shapes of the face layers were generated from the 3D volumes, and were exported in stereolithography (STL) file format for further data analysis.

2.5 Quantification of three-dimensional features

A custom-made 3D feature evaluation routine in MATLAB (2017a, The Mathworks Inc., Natick, Massachusetts, USA) was developed to obtain the detailed sandwich beam structure of the AL with a stereolithography (STL) file of the face layers. The working steps of this routine are outlined below.

To quantify three-dimensional features of the AL in an anatomical frame, the co-registered STL files of the stapes and both face layers were transformed to the anatomical reference frame of *Oxyz*, where the *xy*-plane was fitted to the medial surface of the footplate and the origin *O* was defined as the centroid of the medial surface of the footplate (Sim et al. 2012; 2013).

At each point on the AL, θ_i was defined as an angle counter-clockwise from the positive *x*-axis. Subsequently, the AL could be subdivided into 100 volume sections at equal angular intervals $[\theta_i, \theta_{i+1})$ along its boundary (Fig. 1A).

For each volume section, two local orthogonal axes $\mathbf{n}_i$ and $\mathbf{t}_i$ originating from the section's centroid $\boldsymbol{C}_i$ were determined, and the thickness and width metric were applied along these local axes (see Fig. 1B). This procedure was necessary to ensure that thickness and width were measured properly in each volume section, the angular alignment of which varied along the boundary of the footplate. The importance of this approach can be illustrated by considering a fact that thickness measurements performed along the global *z*-axis in volume sections with a very steep inclination of the face layer would result in a strong bias towards overestimation of the face layer's thickness. The two local measurement axes were obtained with the following rules:

(1) A plane S_i is fitted to the set of points within the corresponding volume section of the face layer.

(2) The vector $\mathbf{n}_i$ is normal to the plane S_i.

(3) The vector $\mathbf{t}_i$ is obtained in fulfillment of all following conditions:

- $\mathbf{t}_i$ lies in the plane S_i
- $\mathbf{t}_i$ is orthogonal to $\mathbf{n}_i$
- $\mathbf{t}_i$ is normal to the inner boundary (i.e., boundary facing the footplate) of the volume section. This orientation was chosen as a good approximation to the fiber alignment in the face layers.
- $\mathbf{t}_i$ is pointing away from the inner to the outer boundary of the volume section.

Once $\mathbf{n}_i$ and $\mathbf{t}_i$ were defined in each volume section, thickness and width in the volume section were calculated in the following way. The two intersection points between the axis $\mathbf{n}_i$ and the triangulated surface of the volume section of the face layer were identified (points ***M*** and ***N*** in Fig. 1B), and the thickness of the face layer was then calculated as the Euclidean distance between the two intersection points (Fig. 1B and 1C). In an analogous fashion, the two intersection points between the axis $\mathbf{t}_i$ and the triangulated surface of the volume section were used to calculate the width of the face layer as the Euclidean distance between the two intersection points (points ***P*** and ***Q*** in Fig. 1B). The thickness of the core layer was measured along the *z*-axis. The total thickness, which indicates a distance from the lateral surface of the face layer on the middle-ear side to the medial surface of the face layer on the cochlear side, was measured along the *z*-axis of the anatomical reference frame as well (Fig. 1C).

In addition to thickness and width measurements, the inclination of the face layer in each volume section was represented by the angle ε_i of $\mathbf{t}_i$ relative to the *xy*-plane of the anatomical frame (Fig. 1C). The angle ε_i was defined to have a positive sign when $\mathbf{t}_i$ was inclined toward the lateral side (i.e., toward to the middle-ear cavity), for volume sections of the face layers both on the middle-ear side (lateral side) and cochlear side (medial side). Then, the relative inclination of the face layer on the middle-ear side with respect to the face layer on the cochlear side could be obtained by

$$\Delta\varepsilon_i = \varepsilon_{Mi} - \varepsilon_{Ci}, \tag{1}$$

where the value ε_{Mi} refers to the inclination of the face layer on the middle-ear side, and ε_{Ci} to the inclination of the face layer on the cochlear side. The difference $\Delta\varepsilon_i$ indicates whether the two face layers are aligned in a divergent, convergent, or parallel alignment pattern relative to each other as they run from the footplate to the cochlear wall. If $\Delta\varepsilon_i > 0$, the two face layers are divergent, while for $\Delta\varepsilon_i < 0$, the two face layers are convergent. A parallel alignment of the two face layers is described by $\Delta\varepsilon_i = 0$.

3. Results

3.1 Visual inspection of multiphoton images

Multiphoton scans of the unstained sample were able to reveal the microstructure of the AL. While tissue excitation was provided by two-photon pulses at 880 nm, resulting emissions from the autofluorescence of elastin (with a wavelength of 483 nm in channel 1) and second-harmonic generation of collagen (with a wavelength of 440 nm in channel 2) were quantified by two photon-counting detectors with a suitable spectral sensitivity. Both detector channels generated outputs with an 8-bit depth, which corresponded to grayscale values of 0-255 per pixel, based on the counted photons. To distinguish between elastin- and collagen-related signals, a different color was assigned to the output of each detector channel (green for elastin-related signals in channel 1 and red for collagen-related signals in channel 2). The complete scanning volumes on the cochlear (Fig. 2A) and middle-ear side (Fig. 2B) are shown with the maximum intensity projection, in which the highest signal intensity along the axis perpendicular to the projection plane is shown. Optical cross sections with a thickness of 10 μm were taken orthogonal to the footplate in the inferior, superior, posterior, and anterior regions. An overview of all cross sections with the maximum intensity projection is provided in Fig. 3A-D for the cochlear side, and in Fig. 3E-H for the middle-ear side of the sample. The cross sections expose five main structures, which can be distinguished based on their signal and morphology: Face layer, core layer, periosteum, stapes, and temporal bone (labels 1-5 in Fig. 3A-H).

The periosteum (▸ 3), a thin soft-tissue layer covering bony surfaces, is predominantly outlined by second harmonics, contrasting the autofluorescence of underlying bone. The face layer (▸ 1) appears as an autofluorescent soft tissue layer connecting the upper part of the stapes (4) and the temporal bone (5). The face layer extended over larger areas of the bony surfaces especially on the cochlear side, which was also observed in a previous work by Davies (1948). In such areas of overlay, it is challenging to clearly distinguish the face layer from periosteum or bone, at least with the employed resolution. Almost no signal emerged from the area below the face layer, with few exceptions of sparse, faint collagen fibers (not shown in the cross sections). It is presumed that this region corresponds to the core layer (2), which has been known to feature a low fiber density and might therefore neither generate sufficient autofluorescence nor second-harmonic generation.

In the maximum intensity projections of the face layers, overall, elastin fibers prevailed, and the relative proportion between elastin and collagen fibers at a given site varied. There was a trend of higher collagen-to-elastin signal ratios in the face layer on the middle-ear side. Such a trend was most pronounced in the anterior region, as shown in Fig. 2B and 3H.

3.2 Quantification of three-dimensional features

Dimensions of the AL were obtained by applying the evaluation routine described in the "Materials and Methods" section to the segmented face layers. Fig. 4 shows the segmented face layers after they were registered to the segmented stapes from the μCT images, and the measured dimensional values are presented in Table 1 and Figs. 5-7.

3.2.1 Thickness of face layers

While the thickness of the face layer on the middle-ear side ranged from 10 to 31 μm (mean of 18 μm), the thickness of the face layer on the cochlear side varied between 7 μm and 18 μm (mean of 10 μm). On the middle-ear side, as shown in Fig. 5A, the face layer exhibited two thickness peaks in the posterosuperior and posteroinferior region, with a local minimum between the peaks. The thickness in the anterior region was found to be higher than inferiorly but did not profoundly differ from the superior region. Trends were more difficult to recognize in the face layer on the cochlear side. On the cochlear side, the thickness around the anterior pole was larger in comparison with the slightly lower thickness in the superior and inferior regions.

Difference of the face-layer thickness between the two sides (thickness on the middle-ear side – thickness on the cochlear side) is shown in Fig. 5B. Generally, the face layer on the middle-ear side was thicker than the face layer on the cochlear side. On average, the face layer on the middle-ear side appeared to be 8 μm thicker than the face layer on the cochlear side, and the thickness of the face layers between the two sides deviated by 23 μm at most.

3.2.2 Width of face layers

The measured width of the face layer on the middle-ear side ranged from 47 to 232 μm (mean of 101 μm), and the width of the face layer on the cochlear side varied between 41 μm and 191 μm (mean of 81 μm).

The width of the face layer on the middle-ear side showed a prominent peak around the anterior pole (see Fig. 6A), with a plateau of larger widths extending to the anterosuperior and anteroinferior region. A smaller second peak was located in the posteroinferior region. The width of the face layer on the cochlear side showed larger values around the anterior pole as well.

Fig. 6B shows the difference of the face-layer width between the two sides (width on the middle-ear side – width on the cochlear side). The two face layers differed in width by an average value of 30 μm, with the largest deviation of 136 μm in the anterosuperior region. In Fig. 6B, the pronounced differences of the width between face layers are located in the

anterosuperior and posteroinferior region, where the face layer on the middle-ear side was much wider than the face layer on the cochlear side. In the posterosuperior region, the face layer on the cochlear side was wider.

3.2.3 Full thickness of the annular ligament

The total thickness of the AL ranged from 142 µm to 471 µm (mean of 289 µm). The largest total thickness was found around the anterior and posterior pole, while the smallest thicknesses occurred in the superior and inferior regions. The total thickness of the AL along the footplate boundary is shown together with the thickness of the core layer in Fig.7. The thickness of the bony annular rim of the sample in this study is shown as well with the corresponding reference data from Sim et al. (2013).

Although the reference data shows a similar relative thickness distribution along the footplate boundary, the overall thickness of the annular rim in the currently investigated sample is considerably larger in all except the inferior region. Furthermore, it should be noted that the total thickness of the AL was mostly exceeding the thickness of the bony annular rim in the sample of this study. This difference between core layer and total thickness was smaller near the inferior region, and larger near the anterior and posterior pole. The smaller differences between core layer and total thicknesses indicate a lower contribution of face layer thickness to total thickness.

3.2.4 Face layer alignment

The angle ε, which is the inclination of the face layer relative to the *xy*-plane as described in the "Materials and Method" section, is shown for both sides in Fig. 8A. As described in the previous section, a positive angle ε denotes an inclination of the face layer toward the middle-ear side while a negative angle ε corresponds to an inclination to the cochlear side.

While a minimal ε of -66° and a maximal ε of 55° were observed (mean of -2°) in the face layer on the cochlear side, the angle ε ranged from -52° to 52° (mean of 18°) in the face layer on the middle-ear side. The difference $\Delta\varepsilon$ of the inclination angle ε between the two sides are shown in Fig. 8B. While the relative alignment of the face layers is mostly convergent or almost parallel around the posterior pole and in the anteroinferior region, all other regions show a divergent alignment of different extents. This is reflected by a positive mean value 20° of $\Delta\varepsilon$ (range between -13° and 64 °).

4. Discussion

The primary focus of this study was to introduce the multiphoton microscopy as a morphometrical tool for quantification of the intact soft-tissue structure of the middle ear. The feasibility of this approach was demonstrated by a preliminary investigation on the AL of the human stapes. The AL was chosen due to its complex three-dimensional geometry and its importance to middle-ear mechanics. It was shown in this study that multiphoton imaging is a suitable modality to quantify morphometry of the complete AL with a complicated three-layer structure.

4.1 Methodological accuracy

There are 3 main sources of error in the presented methodology: 1) Resolution of the optical system, 2) The co-registration between| imaging domains, and 3) Manual segmentation.

Measurement errors in the thickness of face layers can be estimated from the resolution of the multiphoton microscopy in the *Z*-direction, which was set to 990 nm (slightly larger than the 692-nm resolution in the *X*- and *Y*- directions) in this study. The resolution in the *Z*-direction corresponds to 5% of the mean thickness of the face layer on the middle-ear side (18 microns), 9% of the mean thickness of the face layer on the cochlear side, and 13% of the thickness even in the thinnest region (7 microns in the superior region of the face layer on the cochlear side). The resolution in the z-direction occupies only 0.4% of the mean thickness of the core layer (229 microns).

The multiphoton and μCT images were co-registered to obtain dimensions and orientations of the face and core layers with respect to the footplate plane. While the relative inclination between the two face layers was not affected by the co-registration process, inclination of the face layers relative to the footplate plane may differ depending on definition of the footplate plane and accuracy in the co-registration process. The footplate plane defined in this study was obtained such that the plane was best fit to the medial surface of the footplate, which was reconstructed from a high-resolution μCT imaging. Such a definition of the footplate plane can be considered reasonable because with this definition of the footplate plane, the net volume displacements by the rocking-like motion of the footplate are minimized (Sim et al. 2012; 2013). The co-registration process in this study was performed based on a surface-matching algorithm (Align Surface module in Amira). For accuracy of the co-registration process, a sufficient area on the stapes was obtained during the multiphoton microscopy (Fig. 2), and thus even mismatch of 5° between multiphoton and μCT images could be recognized

even by mere visual inspection of the matched surfaces. Therefore, errors during co-registration process would not exceed 1-2°.

The manual segmentation of the face layers of the AL on multiphoton images may result in errors caused by limitations in the precision of manual contouring. However, the clear border between face layer and core layer is expected to drastically reduce errors in thickness measurements, which should therefore not exceed the single-digit micron range. Measurements in width may be subject to higher errors due to the overlap between the face layers and the bony surface of the stapes and the temporal bone. Since the width reported in this study mostly corresponds to the width of the AL bridging the gap between stapes and temporal bone, the related measurement error should not exceed the single-digit micron range due to the clear visibility of the region of the face layer bridging the stapes and the temporal bone.

4.2 Face layer dimensions

In a work by Baek et al. (2015), the face layers on both the middle-ear and cochlear sides were assumed to have a uniform thickness of 20 microns. According to results of this study (Table 1 and Fig. 5), the thickness of the face layer on the middle-ear side is larger than the thickness of the face layer on the cochlear side. While the mean thickness on the middle-ear side (18 microns) was similar to the value in Baek et al., the mean thickness on the cochlear side (10 microns) was just a half of the assumed thickness. The thickness of each face layer showed variation along the footplate boundary as well, with standard deviations of 4.7 microns on the middle-ear side and 2.3 microns on the cochlear side, which correspond to 26% and 23 % of the mean value, respectively. Therefore, the modeling assumption that the thickness of a face layer along its own boundary is constant is not drastically inconsistent with the current data.

The mean widths of the face layers in this study (Table. 1 and Fig. 6) were 101 micron on the middle-ear side and 81 microns on the cochlear side, which are smaller than the mean width in Baek et al. (200 microns on both sides). The variation of the width along the footplate boundary was more pronounced than the variation in thickness. The width variation has standard deviations of 48.1 microns on the middle-ear side and 35.0 microns on the cochlear side, which correspond to 48% and 43 % of the mean value, respectively. The assessment of width was complicated by the fact that face layers may overlap the bony surface of the stapes and the temporal bone. Hence, they cannot be clearly distinguished from periosteum or underlying bone in multiphoton images. Width data presented in this study therefore mostly correspond to the width of the ligament effectively bridging the gap between stapes and temporal bone.

In conclusion, it is noteworthy that 1) the thickness of the face layers is not uniform along the footplate boundary, 2) the thickness and width of the face layer on the middle-ear side are larger than on the cochlear side, and 3) the width has larger variation along the footplate boundary than the thickness.

4.3 Face layer inclination

The inclination of both face layers varied along the footplate boundary. The predominantly divergent alignment of the two face layers in most regions was only contrasted by the almost parallel or slightly convergent alignment in the posterior and anteroinferior region. In previous measurements of spatial stapes motion (Hato et al. 2005; Sim et al. 2009; Lauxmann et al. 2012), it was assumed that fibrous structures are aligned on the footplate plane, and thus in-plane motion of the stapes is minimized due to relatively larger stiffness for elongation and contraction of the fibrous structure. However, as the inclination of the face layers varies along the footplate boundary, the "in-plane" direction may differ along the footplate boundary.

Out of all thirteen (five for divergence, five for convergence, and three for parallel configuration) theoretically possible face layer alignments, only three divergent, one parallel, and one convergent configuration were found in the current sample (Fig. 9). The three different divergent alignment patterns should be distinguished since they provide different amounts of resistance against stapedial motion in a direction-dependent manner. In the first two configurations, the face layers diverge relative to each other, but they both either incline towards the middle-ear side (anterior and anteroinferior region) or the cochlear side (superior and posteroinferior region). Contrarily, in the third configuration (anterosuperior and small segment of posteroinferior region), the face layers are inclined towards opposite sides. The first configuration might provide a higher stiffness for piston-like movements of the stapes out of the cochlea than for movements into the vestibulum, while the opposite is the case for the second configuration. Again, the reason for this assumption is that a displacement of fibers in axial direction results in a higher stiffness than a displacement perpendicular to the fiber axis.

The posterior region mostly featured a parallel or slightly convergent alignment with both face layers inclined towards the middle-ear side. These configurations would predominantly resist stapes motion into the vestibulum upon activation of the stapedial reflex (since more fibers are being pulled in their axial direction). This finding is in good agreement with the work of Brunner (1954), who mentioned that the alignment at the anterior and posterior pole would counteract exceedingly large movements into and out of the vestibulum, respectively. Brunner (1954) additionally suggested that the dimensions of the AL are mainly

determined by the effect of larger forces, such as resulting from the action of the stapedial muscle, while acoustic stimuli were considered too small a force to have an influence on shaping the structure's dimensions.

4.4 Thickness of the core layer

The circumstance that the core layer did not generate a substantial signal in multiphoton scans might be explained by a very low fiber density. The low signal from the region beneath the face layers which has been attributed to the core layer does not solely result from a loss of signal due to limited penetration depth or scattering. This is plausible since a significant amount of signal from the optically much denser bone could be measured even beyond this depth.

The thickness of the core layer as well as the total thickness of the AL could be obtained with the co-registration of both face layers to a μCT scan of the stapes. The maximal total thickness was observed around the anterior and posterior poles of the footplate (Fig. 7). This reflects a similar relative thickness distribution along the footplate boundary as in the reference data from Sim et al. (2013). However, the thickness of the annular rim in the currently investigated sample surpassed the values from the reference data in all but the inferior, anteroinferior and posteroinferior region. This discrepancy can be explained due to several factors: First, a comparably high total thickness of the AL results from the larger thickness of the bony rim in our sample. Second, the upper- and lowermost parts of the AL do not always directly emerge from the upper and lower bony rim. The insertion site can also be observed in zones below or above the rim, such as from the periosteum on the surface of the footplate. This is evident in cross sections of previous histological studies (see e.g. Bolz and Lim 1972). Third, the total thickness was measured close to the mid-distance between stapes and temporal bone. Thus, a steep inclination of the face layer would result in thickness values larger than the thickness of the bony rim. Furthermore, Brunner (1954) recapitulated histological findings by Eysell (1870), who found the total thickness of the AL to be exceeding the thickness of the annular rim. Eysell reported a rim thickness of 420 μm at the posterior pole, where the total thickness amounted to 500 μm. At the anterior pole, he measured a total thickness of 300 μm with a corresponding rim thickness of only 250 μm.

4.5 Stiffness of three-layer structure

The most prominent feature of the AL of the human stapes would be its composition of the face layers and core layer, which is similar to a sandwich beam. As described in Section 1 (Introduction), the sandwich structure, with the same amount of fibers, can achieve a higher bending stiffness than the single-layer structure by increasing the distance between the face

layers (Zenkert 1997). According to a theorem of classical mechanics, the moment of inertia I_1 of the single-layer structure with a rectangular cross-section is determined by,

$$I_1 = \frac{bt^3}{12}, \tag{2}$$

where b and t are the width and thickness of the rectangular cross section. For the sandwich structure, assuming that the bending stiffness is provided only by the face layers, the moment of inertia I_2 is determined by

$$I_2 = \frac{bt_1^3}{12} + d_1^2 bt_1 + \frac{bt_2^3}{12} + d_2^2 bt_2, \tag{3}$$

where t_1 and t_2 are the thicknesses of the upper and lower face layers, d_1 and d_2 are the distances from the neutral axis to the centroids of the upper and lower face layers, and b is the width of the sandwich structure. In the case that $d_1 >> t_1$ and $d_2 >> t_2$, the moment of inertia I_2 in Eq. (3) is approximated as,

$$I_2 \approx d_1^2 bt_1 + d_2^2 bt_2. \tag{4}$$

According to the results of this study, the distance between the face layers (mean of 229 microns) is much larger than the thickness of the face layers (mean of 18 microns on the medial side and 10 microns on the cochlear side). Assuming that the bending stiffness of the AL is provided only by fibrous structures in the face layers, the moment of inertia for bending stiffness with the mean distance between the two face layers is larger by more than 200 times than the moment of inertia with zero distance between the two face layers. This means that the three-layer structure of the AL efficiently provides bending stiffness with a small amount of fibers.

Variation of the bending stiffness along the footplate boundary is presumed to be mainly due to variation in the thickness of the core layer (i.e., distance between the face layers) rather than variation in the thickness of the face layers. In Table 1, the standard deviation of the face layer thickness was 4.7 and 2.3 microns on the medial and cochlear sides, respectively. With this standard deviation, the moment of inertia is changed by approximately 10 %. The standard deviation of the core layer thickness was 85.3 microns. With the standard deviation of the core layer thickness, the moment of inertia becomes larger by twice (in the upper limit) or smaller by a half (in the lower limit).

The relation between the total thickness and the bending stiffness is different from the corresponding relation in single-layer structures. According to Fig. 7, the core thickness and total thickness of the AL become the largest near the anterior and posterior regions and the smallest near the inferior region. If the AL is modeled as a single-layer structure with uniform material, the moment of inertia in the thickest region is larger by approximately 16 times than

the moment of inertia in the thinnest region. However, with the three-layer structure, the maximum moment of inertia is larger by approximately 6 times than the minimum stiffness.

4.6 Fiber composition

The relative content of elastin and collagen fibers in different regions of the AL was reflected by the signal ratio of the two detector channels. As was shown in Fig. 2B and 3H, the face layer on the middle-ear side exhibited a higher collagen-to-elastin signal ratio only near the anterior pole, and elastin fibers are dominant in other regions. Such an observation cannot be generalized across subjects because only one sample (46 years old) was investigated in this study. Further, Harty (1953) reported, from a comparison between samples of a 78-years old and a 26-years old temporal bones, that the elastin fibers are denser in the young subject. Composition of the collagen fibers in the AL was not mentioned in the study, but considering the change of density of the elastin fibers, composition of the two fibers in the face layers might be age-related. Although we first report composition of the collagen and elastin fibers in the AL, further investigations are needed to reveal the composition of the two fiber types across subjects of different age groups. Furthermore, it may be worthwhile to acquire morphometrical data of an animal with an auditory system tuned towards higher frequencies (i.e., rodents or dolphins) to explore the implications of different geometrical properties of the AL for hearing in different frequency ranges.

The two types of fibers observed in the face layers have different mechanical properties. Collagen fibers are known to be highly resistant against elongation along the longitudinal direction (Young's modulus of collagen fibers in elongation is known to be larger than the corresponding Young's modulus of elastin fibers by 100-1000 times depending on the type of collagen) but to be relatively flexible for deformation in other directions while elastin fibers feature elastic recoil and contribute to uniform distribution of stress in tissues and thus being more isotropic for deformation (Ushiki 2002). Considering the mechanical properties of the two types of fibers, it is expected in the collagen-reinforced region that in-plane motion of the footplate on the footplate plane (the motion mainly causes elongation of the fibers along the longitudinal direction) is minimized and the AL is less resistant against motion along the direction normal to the footplate plane. In addition, it needs to be noted that even out-plane motion of the footplate (i.e., motion along the direction normal to the footplate plane) causes considerable elongation of the fibers in the case that the magnitude of the motion becomes comparable to dimensions of the AL. If the observation of the collagen-reinforced anterior region in this study is general across subjects, it may contribute to minimizing an overly large intrusion of the stapes into the vestibulum during the stapedial reflex, which can cause

considerable elongation of the fibers due to the large magnitude, and providing flexibility for stapedial motion out of the footplate plane under lower levels of acoustic stimulation.

In addition to the composition, it has been known that mechanical properties of the fibers may differ across subjects and change by various causes. It was mentioned in a work by Green et al. (2014) that elastin fibers can have an extended life span, but also a low re-synthetization rate, and show a tendency towards calcification (e.g. in atherosclerotic plaques in blood vessels) and changes of mechanical properties upon e.g. exposure to chemicals such as high concentrations of glucose by non-enzymatic glycation in diabetes. Green et al. (2014) reported a change in elastin networks by non-enzymatic glycation resulting in an increase of zero-strain dimensions and elastic modulus. Furthermore, a prior study showed that both collagen and elastin could be stiffened, with the collagen network additionally contracting and thereby introducing differential strains (Liu et al. 1988). Similar effects are conceivable for elastin and collagen fibers in the AL as well, finally decreasing sound conduction to the inner ear by affecting its mechanical properties. These changes are not limited to the example of glycation given before, which is especially relevant for elastin and collagen fibers in blood vessels. Similar changes could e.g. occur upon exposure to soluble substances involved in middle-ear inflammation. Therefore, it might be beneficial to include these aspects in future biomechanical models of the middle ear, and to compare them to changes found in clinical middle-ear measurements which contain some information about mechanical properties of the middle ear.

4.7 Conclusion and outlook

Multiphoton microscopy was introduced as a new imaging modality for the morphometry of an intact soft tissue structure of the human middle ear. The designated pilot application was focusing on the morphometrical analysis of the human AL along its full boundary. A comprehensive workflow ranging from sample preparation to image processing and data analysis was developed for use in this preliminary work and future investigations. The results of the current study indicate that thickness, width, and inclination of both face layers of the AL vary along the footplate boundary. Qualitative and quantitative contributions of the non-uniform distribution of the complicated AL structures to middle-ear mechanics are expected to be revealed when the non-uniform dimensions and orientation of the AL structures are integrated into comprehensive models of the middle-ear ossicular chain. This study aims to provide a methodology for precise description of the AL anatomy. After this initial demonstration of methodological feasibility, a thorough investigation of more samples and potentially other soft tissue structures in the middle-ear will follow.

Acknowledgements

This work was supported by SNF Grant No. 320030-176123. Imaging was performed with support of the Center for Microscopy and Image Analysis, University of Zurich. We thank especially Dr. José María Mateos Melero and Dr. Dominik Hänni for their support for using the equipment.

References

Baek, J.D., Steele, C.R., Yoon, Y.-J. 2015. Human stapedial annular ligament mechanical and geometrical property analysis using a bi-layer tapered beam model. International Journal of Precision Engineering and Manufacturing 16, 1623-1630.

Bolz, E.A., Lim, D.J. 2009. Morphology of the Stapediovestibular Joint. Acta Oto-Laryngologica 73, 10-17.

Brunner, H. 1954. Attachment of the stapes to the oval window in man. A.M.A. Archives of Otolaryngology 59, 18-29.

Davies, D.V. 2007. A Note on the Articulations of the Auditory Ossicles and Related Structures. The Journal of Laryngology & Otology 62, 533-536.

De Greef, D., Buytaert, J.A., Aerts, J.R., Van Hoorebeke, L., Dierick, M., Dirckx, J. 2015. Details of human middle ear morphology based on micro-CT imaging of phosphotungstic acid stained samples. J Morphol 276, 1025-46.

Eysell, A.: Beiträge zur Anatomie des Steigbügels und seiner Verbindungen, Arch. Ohrenh. 5:237, 1870.

Graham, M.D. 1985. The annular ligament attachment to the normal human stapes footplate. A scanning electron microscopic study. The Annals of Otology, Rhinology, and Laryngology 94, 171-5.

Green, E.M., Mansfield, J.C., Bell, J.S., Winlove, C.P. 2014. The structure and micromechanics of elastic tissue. Interface Focus 4, 20130058.

Gussen 1968. Early Lesions of Otosclerosis. Acta Oto-Laryngologica 65, 38-44.

Harty, M. 2007. Elastic Tissue in the Middle-Ear Cavity. The Journal of Laryngology & Otology 67, 723-729.

Hato, N., Stenfelt, S., Goode, R.L. 2003. Three-dimensional stapes footplate motion in human temporal bones. Audiol Neurootol 8, 140-52.

Lauxmann, M., Eiber, A., Heckeler, C., Ihrle, S., Chatzimichalis, M., Huber, A., Sim, J.H. 2012. In-plane motions of the stapes in human ears. J Acoust Soc Am 132, 3280-91.

Liu, S.Q., Fung, Y.C. 1988. Zero-stress states of arteries. Journal of Biomechanical Engineering 110, 82-4.

Mohammadi, A., Jufas, N., Sale, P., Lee, K., Patel, N., O'Leary, S. 2017. Micro-CT analysis of the anatomical characteristics of the stapedial annular ligament. Anat Sci Int 92, 262-266.

Neudert, M., Bornitz, M., Lasurashvili, N., Schmidt, U., Beleites, T., Zahnert, T. 2016. Impact of Prosthesis Length on Tympanic Membrane's and Annular Ligament's Stiffness and the Resulting Middle Ear Sound Transmission. Otol Neurotol 37, e369-76.

Sim, J.H., Chatzimichalis, M., Lauxmann, M., Roosli, C., Eiber, A., Huber, A.M. 2010. Complex stapes motions in human ears. J Assoc Res Otolaryngol 11, 329-41.

Sim, J.H., Chatzimichalis, M., Roosli, C., Laske, R.D., Huber, A.M. 2012. Objective assessment of stapedotomy surgery from round window motion measurement. Ear Hear 33, e24-31.

Sim, J.H., Roosli, C., Chatzimichalis, M., Eiber, A., Huber, A.M. 2013. Characterization of stapes anatomy: investigation of human and guinea pig. J Assoc Res Otolaryngol 14, 159-73.

Takanashi, Y., Shibata, S., Katori, Y., Murakami, G., Abe, S., Rodriguez-Vazquez, J.F., Kawase, T. 2013. Fetal development of the elastic-fiber-mediated enthesis in the human middle ear. Ann Anat 195, 441-8.

Ushiki, T. 2002. Collagen fibers, reticular fibers and elastic fibers. A comprehensive understanding from a morphological viewpoint. Archives of histology and cytology 65, 109-26.

Zenkert, D., Fund, N.I. 1997. The Handbook of Sandwich Construction. Engineering Materials Advisory Services.

Figure 1

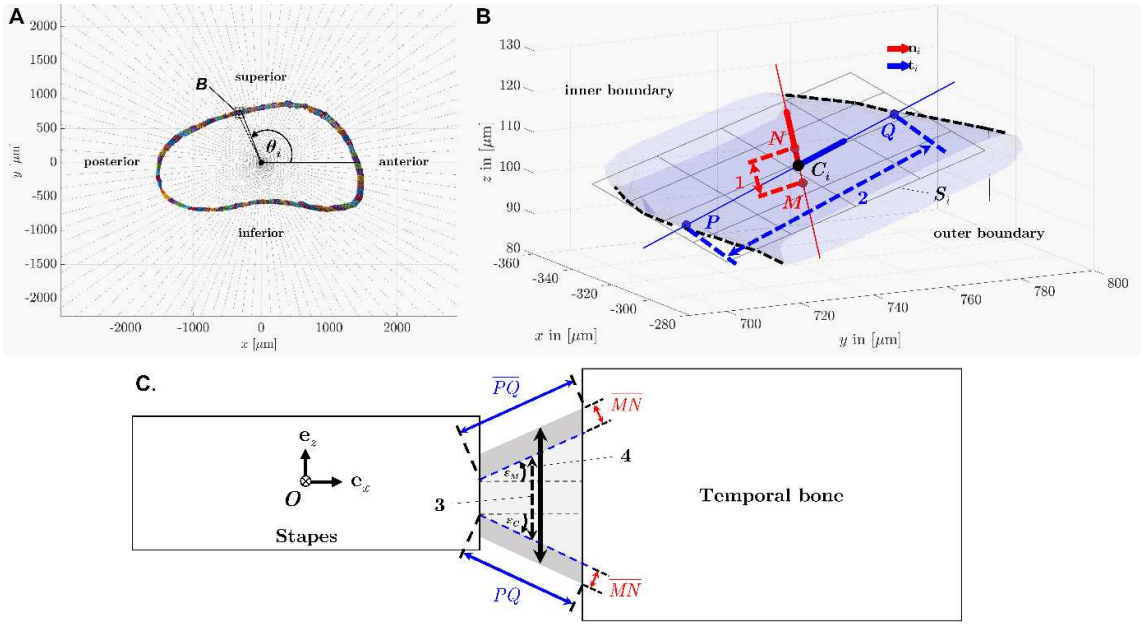

Fig. 1. Schematic illustration of the 3D feature evaluation routine. **A** Subdivision of the face layer on the cochlear side into 100 volume sections at equal angular intervals $[\theta_i, \theta_{i+1})$. **B** Visualization of thickness and width measurements based on a volume section of the cochlear face layer (magnified segment from panel A), and **C** Overview of calculated parameters. $\boldsymbol{C}_i$: centroid of the volume section, S_i: plane fitted to the volume section, $\mathbf{n}_i$: vector normal to S_i originating from the centroid $\boldsymbol{C}_i$, $\mathbf{t}_i$: vector tangent to S_i originating from the centroid $\boldsymbol{C}_i$, $\boldsymbol{\varepsilon}$: inclination angle of the face layer, (1): thickness of face layer, (2): width of the face layer, (3) thickness of the core layer, and (4) total thickness.

Figure 2

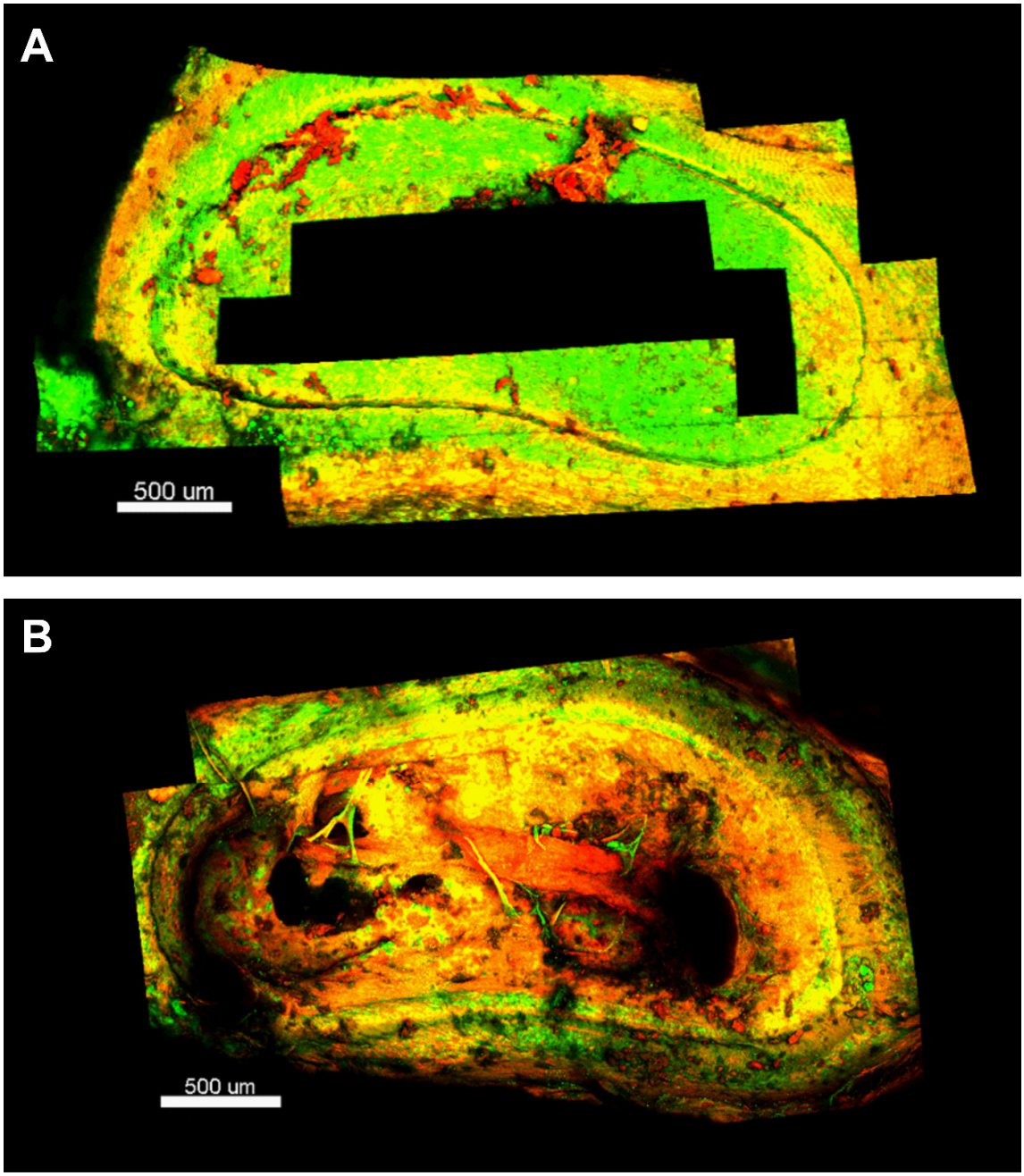

Fig. 2. Maximum intensity projection of the complete scanning volumes **A** on the cochlear side, and **B** on the middle-ear side.

Figure 3

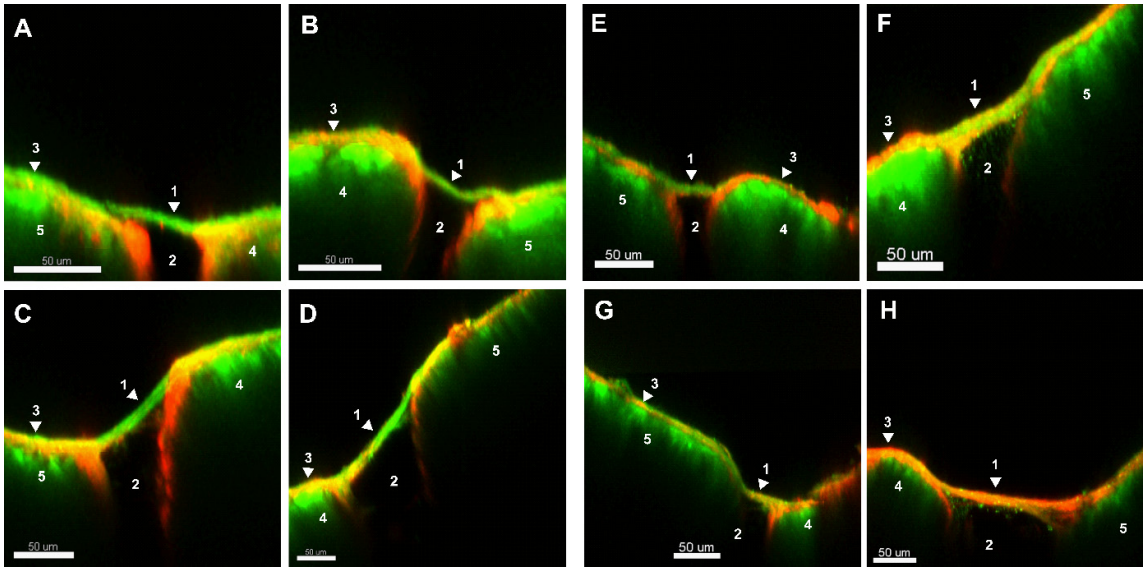

Fig. 3. Optical cross sections for different regions of the cochlear side in the **A** inferior, **B** superior, **C** posterior, **D** anterior regions on the cochlear side, and in the **E** inferior, **F** superior, **G** posterior, **H** anterior regions on the middle-ear side

Figure 4

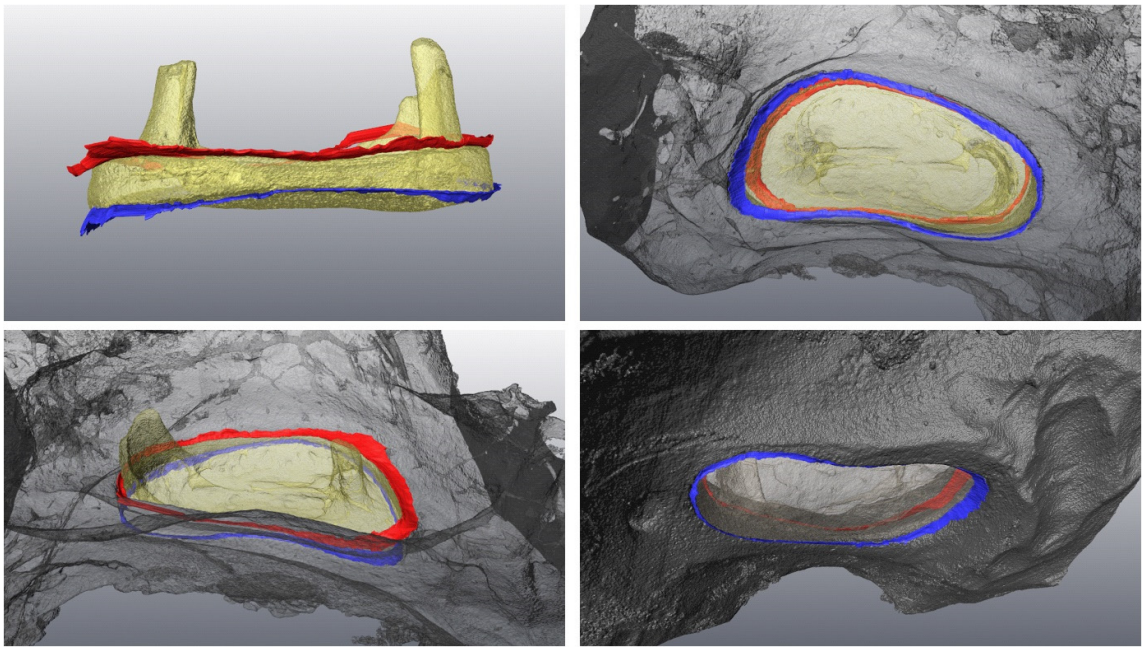

Fig. 4. Segmented face layers (the middle-ear side in red and the cochlear side in blue) after registration to the segmented stapes and peripheral bones from the μCT images.

Figure 5

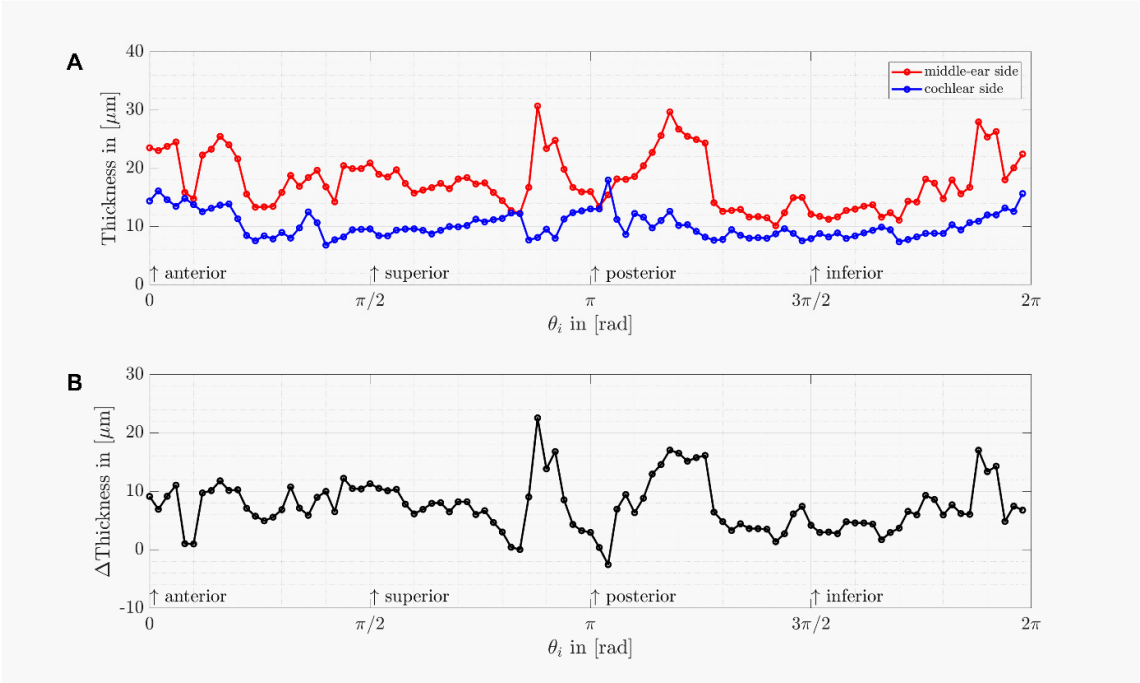

Fig. 5. Thickness of the face layers. **A** Thickness of the face layers on the cochlear and middle-ear side, and **B** Difference of the face-layer thickness between the two sides.

Figure 6

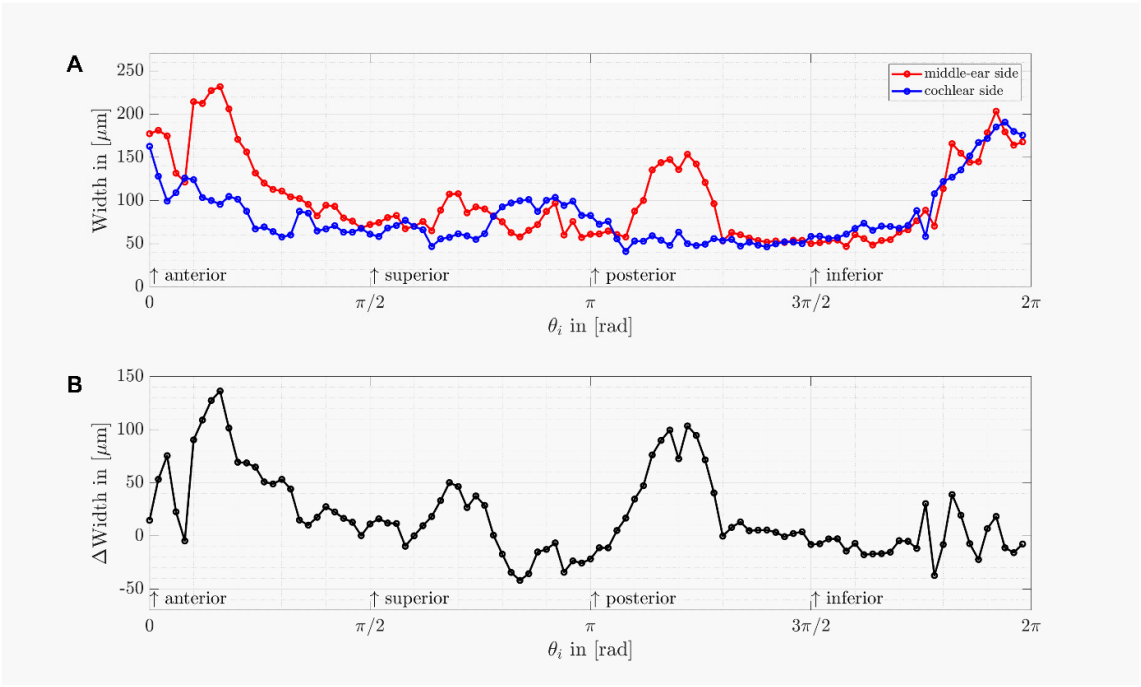

Fig. 6. Width of the face layers. **A** Width of the face layers on the cochlear and middle-ear side, and **B** Difference of the face-layer width between the two sides.

Figure 7

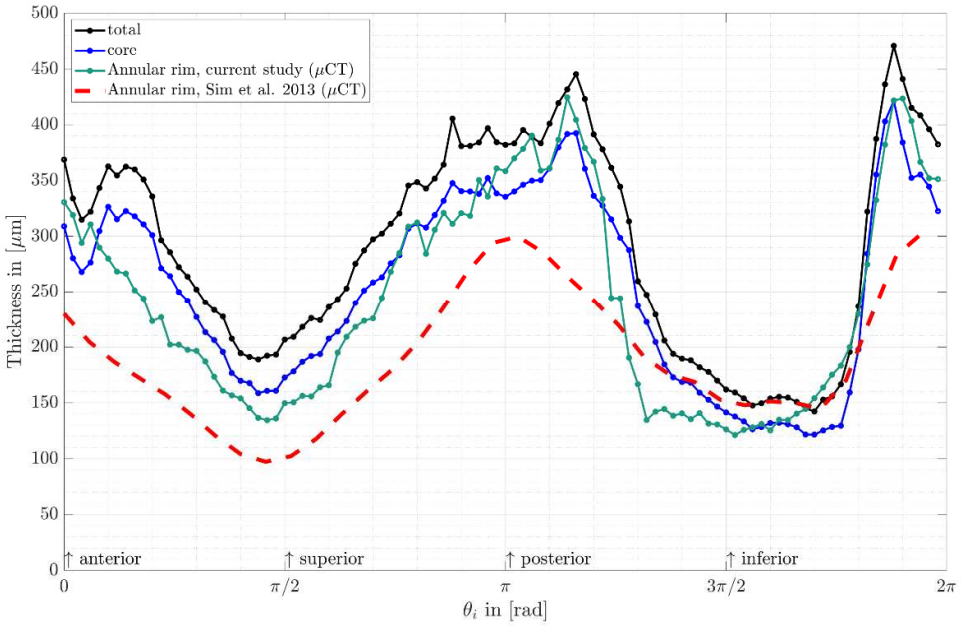

Fig. 7. Total thickness, thickness of the core layer, and thickness of the bony annular rim of the annular ligament with reference data for thickness of the bony annular rim from Sim et al. (2013).

Figure 8

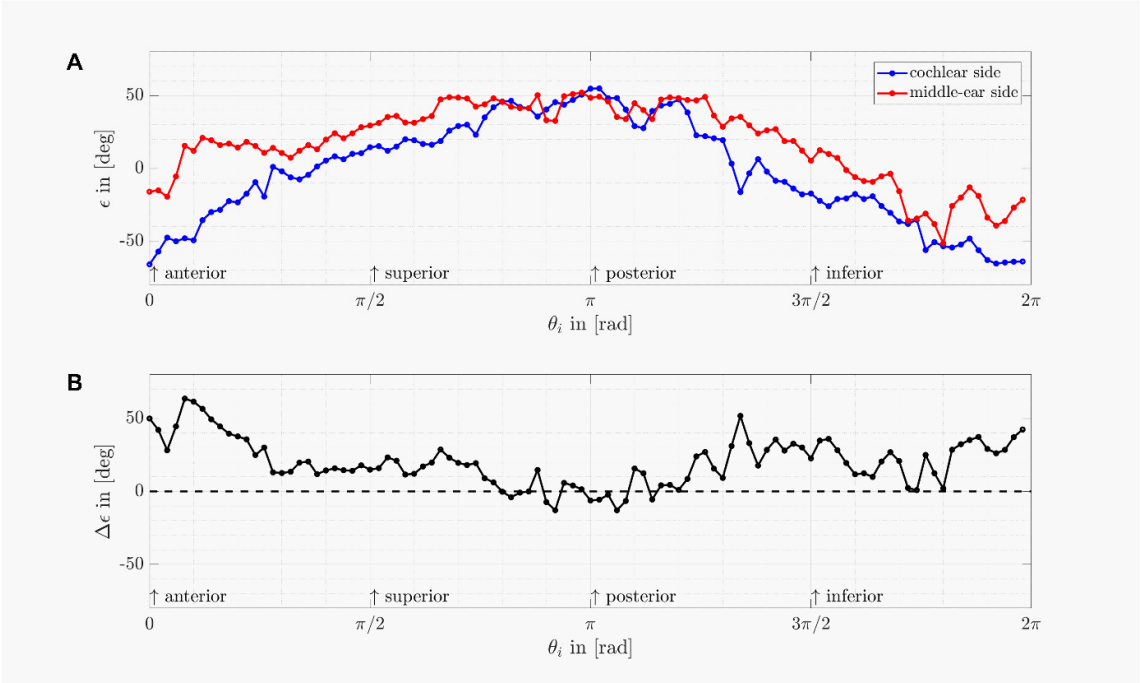

Fig. 8. Inclination of the face layers. **A** Inclination angle ε of cochlear and middle-ear face layer relative to the *xy*-plane, and **B** Difference $\Delta\varepsilon$ of the inclination angle ε between the two sides.

Figure 9

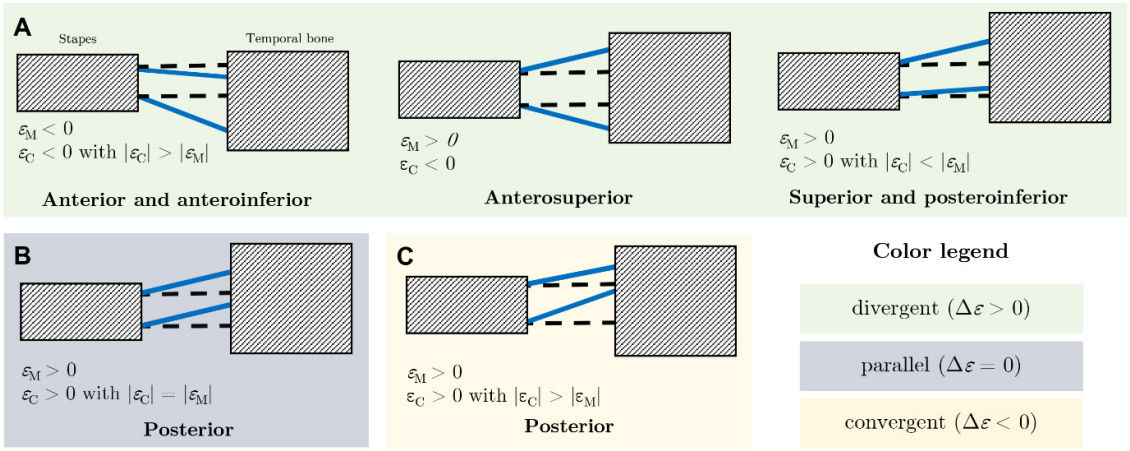

Fig. 9. Relative angular alignment of the two face layers in the sample of this study. **A** Divergent, **B** Parallel, and **C** Convergent.

Table 1. Thickness, width, and angular inclination of the annular ligament.

	Minimum in [µm]	Maximum in [µm]	Mean in [µm]	Standard deviation in [µm]
Thickness				
middle-ear face layer	10 (inferior)	31 (posterosuperior)	18	4.7
cochlear face layer	7 (superior)	18 (posterior)	10	2.3
difference	0 (posterosuperior)	23 (posterosuperior)	8	
core thickness	55 (inferior)	376 (posteroinferior)	229	85.3
total thickness	142 (inferior)	471 (anteroinferior)	289	94.0
Width				
middle-ear face layer	47 (inferior)	232 (anterosuperior)	101	48.1
cochlear face layer	41 (posterior)	191 (anterior)	81	35.0
difference	0 (superior)	136 (anterosuperior)	30	
Face layer alignment				
middle-ear face layer	-52° (anteroinferior)	52° (posterior)	18°	
cochlear face layer	-66° (anterior)	55° (posterior)	-2°	
alignment between face layers	-13° (posterior)	64° (anterosuperior)	20°	